Unraveling radial dependency effects in fiber thermal drawing

Cite as: Appl. Phys. Lett. **115**, 044102 (2019); https://doi.org/10.1063/1.5109469
Submitted: 09 May 2019 . Accepted: 08 July 2019 . Published Online: 26 July 2019

Alexis G. Page, Mathias Bechert, François Gallaire, and Fabien Sorin

Applied Physics Letters ARTICLE scitation.org/journal/apl

Unraveling radial dependency effects in fiber thermal drawing

Cite as: Appl. Phys. Lett. **115**, 044102 (2019); doi: 10.1063/1.5109469
Submitted: 9 May 2019 · Accepted: 8 July 2019 ·
Published Online: 26 July 2019

Alexis G. Page,[1,a)] Mathias Bechert,[2,a)] François Gallaire,[2] and Fabien Sorin[1,b)]

AFFILIATIONS

[1]Laboratory of Photonic Materials and Fibre Devices, École Polytechnique Fédérale de Lausanne, 1015 Lausanne, Switzerland
[2]Laboratory of Fluid Mechanics and Instabilities, École Polytechnique Fédérale de Lausanne, 1015 Lausanne, Switzerland

[a)]**Contributions:** A. G. Page and M. Bechert contributed equally to this work.
[b)]**Electronic mail:** fabien.sorin@epfl.ch

ABSTRACT

Fiber-based devices with advanced functionalities are emerging as promising solutions for various applications in flexible electronics and bioengineering. Multimaterial thermal drawing, in particular, has attracted strong interest for its ability to generate fibers with complex architectures. Thus far, however, the understanding of its fluid dynamics has only been applied to single material preforms for which higher order effects, such as the radial dependency of the axial velocity, could be neglected. With complex multimaterial preforms, such effects must be taken into account, as they can affect the architecture and the functional properties of the resulting fiber device. Here, we propose a versatile model of the thermal drawing of fibers, which takes into account a radially varying axial velocity. Unlike the commonly used cross section averaged approach, our model is capable of predicting radial variations of functional properties caused by the deformation during drawing. This is demonstrated for two effects observed, namely, by unraveling the deformation of initially straight, transversal lines in the preform and the dependence on the draw ratio and radial position of the in-fiber electrical conductivity of polymer nanocomposites, an important class of materials for emerging fiber devices. This work sets a thus far missing theoretical and practical understanding of multimaterial fiber processing to better engineer advanced fibers and textiles for sensing, health care, robotics, or bioengineering applications.

Thermal drawing is at the heart of the fabrication of telecommunication optical fibers. As illustrated in Figs. 1(a) and 1(b), it consists in heating a macroscale preform, typically made out of glass or thermoplastics, to its softening temperature and pulling it to create a much thinner and longer fiber that maintains the initial cross-sectional architecture. From simple glass-based step index structures, the design of optical fibers was expanded to single-mode waveguiding, photonic crystals, and Bragg mirror fibers.[1–7] This technique has also been used to make microstructured multimaterial fibers that integrate optical, electronic, and optoelectronic materials.[7–11] These fibers exhibit advanced functionalities,[9,12] making them promising building blocks for applications in not only optics but also soft electronics,[13–16] optoelectronics,[10,11,13,17,18] sensing,[16,19] or bioengineering.[19–21]

While the introduction of different materials in the drawing process has triggered much interest to realize innovative fiber-based devices and smart textiles, subtle effects of the fluid dynamics of multimaterial codrawing remain to be investigated to better understand and exploit this approach. In particular, modeling and analytical analysis have mostly relied on fluid dynamics descriptions that assume a velocity in the drawing direction that is independent of the radial position.[19,22,23] There exist some numerical studies that are not based on such an assumption, but only in the context of single material, microstructured optical fibers.[23,24] The impact of the nonuniform velocity field in the cross section in the context of multimaterial drawing is however essential, albeit yet unexplored. A radially varying velocity field and hence deformation rate during drawing can influence the targeted architecture and the resulting properties of the functional materials at the fiber level. A striking manifestation of this effect is schematically shown in Fig. 1(a), where initially rectangular domains of polymer nanocomposites deform significantly during drawing. The pattern observed, which we experimentally show and model below, results from a relative displacement of material at different radial positions. Taking this effect into account is primordial to realize advanced fiber-based devices with controlled properties.

In this work, we report an in-depth fluid dynamics analysis of the thermal drawing process that takes into account the radial dependency of the axial velocity. We propose a model that includes higher order terms of the velocity field, which enables us to elucidate the

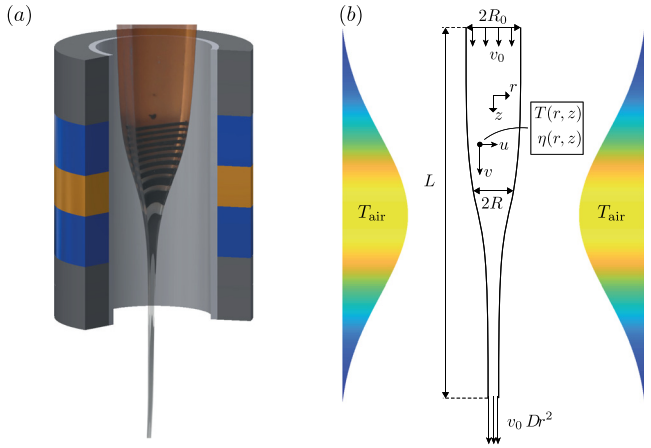

FIG. 1. (a) Visualization of the thermal drawing of a fiber in a furnace with three heating zones. We combined a picture of an interrupted draw with a schematic of the furnace. (b) Sketch of the axisymmetric model. The ambient temperature T_{air} is assumed to have a Gaussian shape along the z-axis.

observation of line deformation shown in Fig. 1(a). From this velocity field, we can extract a more accurate distribution of the rate of deformation during drawing, which is crucial for many material properties at the fiber level. In particular, we apply the results of our model to precisely account for the dependence of electrical conductivity of polymer nanocomposites on the radial position and the draw ratio, i.e., the ratio of preform to fiber diameters. Conductive polymer composites form an important class of materials widely used in fiber-based devices for optoelectronics,[10,17,18] bioengineering,[20,21] and electromechanical sensing.[15,25] They, however, have a well-known, yet so far unexplained dependence of their electrical conductivity on the fiber drawing conditions.[14] Our model advances the understanding of multimaterial fiber drawing and opens opportunities for the design of advanced fiber-based devices and smart textiles with optimum control over the material microstructure.

We extend the reduced one-dimensional model for elongating fibers widely used in the literature[26–29] to cover thermal effects and to access information about the radial distribution of the variables. We consider only the cladding material in the model, as the functional materials represent only a small fraction of the fiber cross-sectional area, and assume an axisymmetric, round fiber. A detailed derivation of the equations is given in the supplementary material. As shown in Fig. 1(b), the fiber can be described by its radius $R(z)$ along the main axis together with the flow velocity field (u, v), with $u(r, z)$ and $v(r, z)$ denoting the radial and axial velocity components, respectively, as well as temperature $T(r, z)$ and shear viscosity $\eta(r, z)$. All variables are made dimensionless using the initial feeding speed v_0, the drawing length L, maximum air temperature T_{max}, and corresponding minimum viscosity η_{min} as reference values. Assuming a slender fiber,[29,30] i.e., $\alpha^2 = (R_0/L)^2 \ll 1$, enables us to expand the variables in α^2, e.g.,

$$v(r,z) = v^{(0)} + \alpha^2 v^{(1)} + \mathcal{O}(\alpha^4), \tag{1}$$

with the superscript indicating the order of expansion. Using an effective drawing length of $L = 40$ cm and an initial radius of $R_0 = 1.25$ cm, $\alpha^2 = \mathcal{O}(10^{-3})$.

Following a previous study,[31] we assume a parabolic temperature field in r,

$$T^{(0)}(r,z) = \left\langle T^{(0)} \right\rangle + Bi\,\frac{\left(\langle T^{(0)}\rangle - T_{air}\right)R}{4 + Bi\,R}\left(1 - 2\,\frac{r^2}{R^2}\right), \tag{2}$$

which enables us to calculate the cross section averaged governing equations. The cross section average is denoted by $\langle\cdot\rangle$, and the Biot number, which compares the heat exchange between the material and the surrounding air to the heat conduction within the fiber, is defined by $Bi = R_0\,h/k$, with h being the heat transfer coefficient and k the material heat conductivity. Note that Eq. (2) implicitly assumes that the preform is primarily heated by the surrounding air, even though weak radiative heating can be accounted for by using this approach as well.[32] In some thermal drawing processes, radiative heating can lead to a material temperature higher than the air temperature,[33] which cannot be modeled by this approach. Similarly, some functional materials may change the mechanical and heat properties of the fiber significantly, despite their low proportion inside the fiber.

For the description of the surrounding air temperature, we assume a centered Gaussian profile,

$$T_{air}(z) = \frac{\Lambda \exp\left[-\dfrac{(z-0.5)^2}{\Delta^2}\right] + 1}{\Lambda + 1}, \tag{3}$$

with dimensionless amplitude Λ and width Δ.

Utilizing the expansion in α^2, the steady state leading order equations are obtained by cross section averaging the continuity, momentum and heat equations, which yields

$$\partial_z\left(R^2\,v^{(0)}\right) = 0, \tag{4a}$$

$$\partial_z\left(R^2\,\langle\eta^{(0)}\rangle\,\partial_z v^{(0)}\right) = 0, \tag{4b}$$

$$v^{(0)}\partial_z\langle T^{(0)}\rangle = -St\,\frac{\langle T^{(0)}\rangle - T_{air}}{R(1 + Bi\,R/4)}, \tag{4c}$$

with radially independent axial velocity $v^{(0)} = v^{(0)}(z)$. The Stanton number St compares the heat transfer between the fiber and the surrounding air with the heat advected by the polymer flow and is given by $St = 2\,Bi/(\alpha\,Pe)$, with the Peclet number $Pe = \rho\,c_p\,v_0\,R_0/k$, c_p denoting the heat capacity of the material. The energy equation (4c) is coupled to the momentum equation (4b) using Arrhenius' law,

$$\eta = \exp\left[\mu\left(\frac{1}{T} - 1\right)\right], \tag{5}$$

with μ being the dimensionless activation energy. The streamwise boundary conditions are given by the process setup as

$$v^{(0)}(0) = R(0) = 1, \quad \langle T^{(0)}\rangle(0) = T_{air}(0), \tag{6a}$$

$$v^{(0)}(1) = Dr^2, \tag{6b}$$

with the draw ratio Dr defined by the ratio of preform to fiber diameters. h, Λ, and Δ are determined using the experimentally determined preform-to-fiber radius profile during drawing. A detailed description of the parameter determination procedure is given in the supplementary material.

We solve Eqs. (4)–(6), which will also be referred to as the "cross section averaged model" in the following, by numerical continuation

using AUTO97[34] to obtain R, $v^{(0)}$, $u^{(0)} = -r\,\partial_z v^{(0)}/2$, $\langle T^{(0)}\rangle$, and $\langle \eta^{(0)}\rangle$. Using these solutions, we then go beyond the usual analysis by calculating the radially varying $T^{(0)}$ and $\eta^{(0)}$, as well as investigating the α^2-order of the expanded governing equations, which yield

$$\partial_r\left[\eta^{(0)} r\left(\partial_r v^{(1)} - \frac{r}{2}\partial_{zz} v^{(0)}\right)\right] = -3\,r\,\partial_z\left(\eta^{(0)}\partial_z v^{(0)}\right). \quad (7)$$

Equation (7) can be solved by numerical integration to obtain $v^{(1)}$ and $u^{(1)} = \int_0^r dr\,(r\,\partial_z v^{(1)})/r$, depending on both r and z.

To demonstrate the importance of this last step, we calculate the evolution of an initially straight line perpendicular to the drawing direction during the drawing process. Figure 2(a) shows the line shape at several axial positions along the fiber within the domain of deformation. Using only the cross section averaged model (black dashed lines), an initially straight line remains straight during the entire process, which is not surprising as the dominating axial velocity does not vary along the radius at leading order. However, if the higher order terms $u^{(1)}$ and $v^{(1)}$ are included in the calculation (red lines), the lines clearly deform during the drawing, finally looking like an inverted "V."

In order to visualize this effect experimentally, we fabricate (see the supplementary material) a polysulfone (PSu) preform of rectangular cross section (2.5 cm × 1.4 cm) within which 1 mm-wide sheets of carbon-black-loaded polycarbonate (PC) are equidistantly placed,

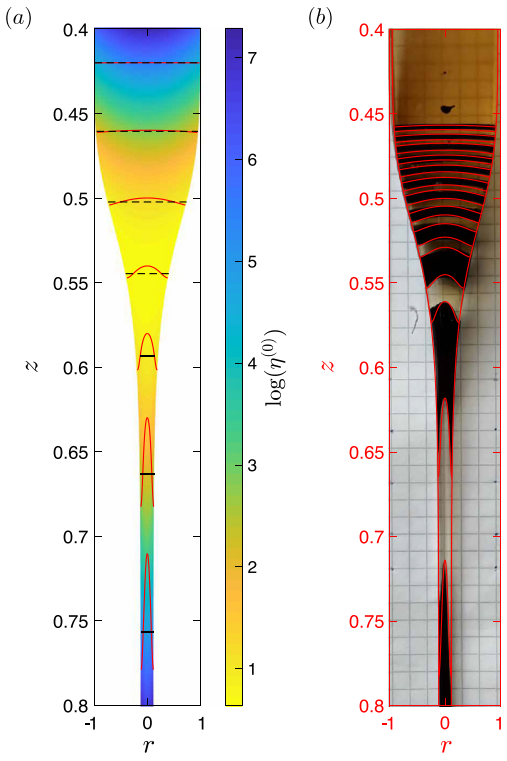

FIG. 2. Effect of higher order terms on the evolution of initially straight material lines during the drawing process. (a) The black dashed lines are calculated with the cross section averaged model, while the red lines result from the full model. The color map shows the logarithm of the dimensionless viscosity. (b) Comparison of theoretical prediction (red lines) with experimental observation for a PSu fiber. Parameters: $Dr = 8.31$, $Bi = 1$, $St = 32$, $\mu = 53$, $\Lambda = 0.5$, and $\Delta = 0.22$.

perpendicular to the drawing direction. The feeding speed is set to 2 mm/s, and the draw ratio is $Dr = 8.31$. The furnace has three heating zones [see Fig. 1(a)], which are set to 200/300/120 °C. The drawing of this preform is interrupted so that the sheets visualize the deformation of initially straight, horizontal material lines during drawing, as shown in Fig. 2(b).

The calculated (red) lines coincide very well with the observed shape of the sheets in the PSu fiber. Note that this comparison is nevertheless of qualitative nature, as the fiber used in the experiment has a rectangular cross section, while the model assumes a circular fiber. A PC fiber is found to yield less quantitative but still qualitative coincidence with the model prediction, which is probably due to the simplification of heating mechanisms as discussed above. For both materials, however, the final shape of the deformed lines is reproduced with high accuracy. All the parameter values are given in the caption of Fig. 2. Physically, the nonuniform propagation of fluid elements lying on an initially straight line is the result of an interplay between a radially varying viscosity [see Fig. 2(a) and the supplementary material] and the deformation of the fiber due to drawing.

It is worth mentioning that the significant influence of the higher order velocity terms is a cumulative effect. At one particular position in z, the change in velocity introduced by the higher order is at most only a few percent. This is expected, as the contribution is scaled by α^2 according to Eq. (1), with α^2 being small at the basis of the expansion. By following a material point during the drawing, however, we integrate along the fiber length, and by that the order of magnitude increases from $\alpha^2 = (R_0/L)^2$ to R_0^2/L. For this reason, the widely used cross section averaged model, Eqs. (4)–(6), is well-suited if one is interested exclusively in the fiber radius and the averaged velocity field, as it is the case for single-material fibers, but insufficient if radially distributed properties come into play, like for multimaterial fibers.

To further highlight the importance of this understanding, we now investigate the influence of thermal drawing on the electrical conductivity of nanocomposites. As conductive fillers, we use carbon black (CB) and carbon nanotubes (CNT). In particular, we fabricate two types of preform: a PSu cladding with a PC-CNT composite sheet and a PC cladding with a PC-CB composite sheet. For drawing the preform with PSu cladding, we use the same settings as above. The preform with PC cladding has a rectangular cross section (2.5 cm × 2.3 cm), the feeding speed is set to 2 mm/s, and the heating zones of the furnace are set to 120/270/120 °C.

As visible in Figs. 3(a) and 3(b), the nanocomposite sheet is in contact with several metallic ribbons (2 mm × 1 mm cross section) made of a bismuth-tin (tin-zinc) alloy for the PC (PSu) cladding. Even though the ribbons melt during consolidation and drawing, the high viscosities of the cladding and sheet materials ensure that the cross-sectional architecture is preserved. By polishing away the cladding of the drawn fiber, we can connect the metallic electrodes to a multimeter to measure the sheet conductivity perpendicular to the drawing direction [see Fig. 3(a)].

In order to access theoretically the final conductivity, we use a simple percolation law to link the effective filler concentration p_e to the conductivity σ,

$$\sigma = \sigma_{\text{in}}\left(\frac{p_e - p_c}{p_{\text{in}} - p_c}\right)^c, \quad (8)$$

with σ_{in} being the initial conductivity of the undeformed material having an initial filler concentration p_{in}, critical concentration p_c, and

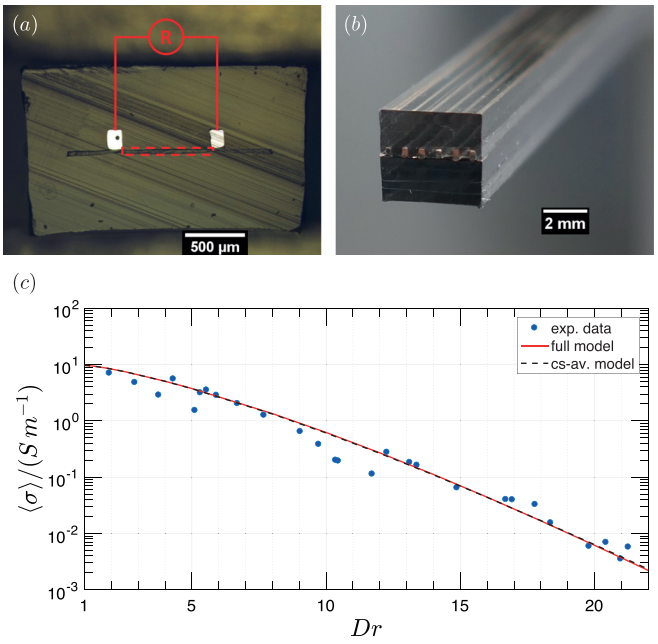

FIG. 3. (a) Optical micrograph of the cross section of a fiber with PSu cladding, PC-CNT composite layer, and two metallic electrodes, which enable us to measure the transversal electrical conductivity for the domain marked by the dashed line. (b) Perspective view of a fiber with PC cladding, PC-CB composite layer, and six metallic electrodes distributed in the cross section. (c) Averaged conductivity of the PC-CNT composite sheet in a multimaterial fiber with a PSu cladding as a function of draw ratio. The perpendicular conductivity is measured between two electrodes placed at $r/R = \pm 0.6$, as shown in (a). Blue points show the experimental data, while the red and black, dashed lines depict the theoretical prediction of the full and cross section averaged models, respectively. Parameters: $Bi = 1$, $St = 32$, $\mu m = 53$, $\Lambda = 0.5$, $\Delta = 0.22$, $m = 1.5$, $\sigma_{in} = 9.7\,\mathrm{S\ m^{-1}}$, $ac = 3.9 \times 10^{-3}$ (full model), and $ac = 3.6 \times 10^{-3}$ (cross section averaged model).

critical exponent c. To account for the destruction of conductive pathways due to deformation during drawing, we propose an empirical kinetic equation inspired by a previous work,[35] which links the effective filler concentration to the second invariant of the deformation tensor $\sqrt{II_D}$ (see the supplementary material),

$$\partial_t p_e = -a\,\eta\,\sqrt{II_D}^{\,m}(p_e - p_c). \tag{9}$$

a denotes a destruction rate, and analogous to the previous work,[35] we set $m = 1.5$. Solving Eq. (9) and substituting in (8) then yield

$$\sigma(r_f) = \sigma_{in} \exp\left(-a\,c \int_{\gamma(r_f)} \frac{dz}{v}\,\sqrt{II_D}^{\,m}\,\eta\right), \tag{10}$$

with $\gamma(r_f)$ denoting the trajectory of a material element during drawing with final radial position r_f. The values of ac and σ_{in} are determined by fitting the experimental data. Equation (10) yields the radial distribution of conductivity in the drawn fiber, which can then be used to calculate the averaged conductivities measured between two electrodes [see Fig. 3(a)].

Figure 3(c) shows the perpendicular conductivity of the PC-CNT composite in a PSu fiber, measured between two electrodes placed at $r/R = \pm 0.6$ for a large range of draw ratios, and compares it to the theoretically determined averaged conductivity (red line). The increased deformation due to a larger draw ratio leads to a change in conductivity over several orders of magnitude, which is well reproduced by our model. Also plotted is the theoretical prediction based on the cross section averaged model (black dashed line). Both models lead to practically identical results, which is not surprising as we average the conductivity over a large part of the fiber radius.

In order to access experimentally the conductivity as a function of the radial position, we prepare a PC/PC-CB preform with six electrodes placed at equal distances along the fiber width [see Fig. 3(b)]. Figure 4 shows the measured conductivities for two different draw ratios. The points are placed in the middle of the domain of average, which has a size of 2.5 mm, i.e., 0.25 R, corresponding to the distance between the electrodes. These measurements are compared with the theoretically obtained moving-averaged distribution (red line). Despite its simple approach, our model describes the variation of conductivity along the radial position very well. Note that analogous to the PSu/PC-CNT fiber, the values of σ_{in} and ac are uniquely set, independent of the draw ratio. Also shown in Fig. 4 is the averaged conductivity distribution resulting from the cross section averaged model (black dashed line). Clearly, this model is incapable of predicting such a large radial variation of the conductivity, emphasizing the need of our extended model.

The model presented here is able to predict the radial distribution of material properties in multimaterial fibers fabricated by weakly radiative thermal drawing, while it maintains the simplicity and flexibility of the cross section averaged one-dimensional model for

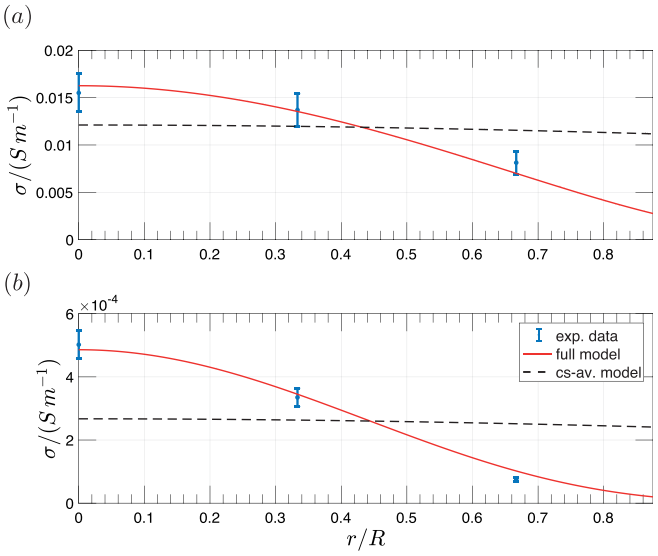

FIG. 4. Dependence of the conductivity on the fiber radius for a PC-CB composite sheet in a multimaterial fiber with a PC cladding for two draw ratios, (a) $Dr = 5.12 \pm 0.16$ and (b) $Dr = 7.24 \pm 0.13$. The blue points depict the experimentally determined conductivities calculated by averaging 3–10 measurements of the perpendicular conductivity between two metallic electrodes for each point. The error bars correspond to the standard deviation. The red line shows the theoretically predicted radial distribution of the averaged conductivity, and the black, dashed line depicts the distribution obtained using only the cross section averaged model. Parameters: $Bi = 1.5$, $St = 27$, $\mu = 48$, $\Lambda = 0.45$, $\Delta = 0.17$, $m = 1.5$, $\sigma_{in} = 2\,\mathrm{S\,m^{-1}}$, $ac = 1.1 \times 10^{-2}$ (full model), and $ac = 9.8 \times 10^{-3}$ (cross section averaged model).

single-material fibers. Even though assumptions like using a circular cross section or employing the simple empirical kinetic equation (9) appear to be rather strong, we are able to reach qualitative and quantitative coincidence with our experimental findings. The flexibility of the model enables comprehensive parametric studies to find routes to innovative experimental designs. Our approach improves the understanding of multimaterial fiber drawing and opens opportunities for the design of advanced fiber-based devices with optimum control over the material microstructure and tailored properties.

See the supplementary material for a detailed derivation of the thermal drawing model, a description of the materials and experimental methods used in this work, all parameter values used in the modeling, together with a description of how they are obtained, and further information on the evolution of material temperature, viscosity, and velocity fields during drawing.

REFERENCES

[1]M. G. Kuzyk, U. C. Paek, and C. W. Dirk, "Guest-host polymer fibers for nonlinear optics," Appl. Phys. Lett. **59**, 902–904 (1991).

[2]M. A. van Eijkelenborg, M. C. J. Large, A. Argyros, J. Zagari, S. Manos, N. A. Issa, I. Bassett, S. Fleming, R. C. McPhedran, C. M. de Sterke, and N. A. P. Nicorovici, "Microstructured polymer optical fibre," Opt. Express **9**, 319–327 (2001).

[3]A. Yeung, K. Chiang, V. Rastogi, P. Chu, and G. Peng, "Experimental demonstration of single-mode operation of large-core segmented cladding fiber," in *Optical Fiber Communication Conference*, *OFC* (IEEE, 2004), Vol. 2.

[4]G.-D. Peng, P. N. Ji, and T. Wang, "Development of special polymer optical fibers and devices," in *Active and Passive Optical Components for WDM Communications IV* (International Society for Optics and Photonics, 2004), Vol. 5595, pp. 138–153.

[5]A. Argyros, "Microstructured polymer optical fibers," J. Lightwave Technol. **27**, 1571–1579 (2009).

[6]M. A. Schmidt, A. Argyros, and F. Sorin, "Hybrid optical fibers: An innovative platform for in-fiber photonic devices," Adv. Opt. Mater. **4**, 13–36 (2016).

[7]W. Yan, A. Page, T. Nguyen-Dang, Y. Qu, F. Sordo, L. Wei, and F. Sorin, "Advanced multimaterial electronic and optoelectronic fibers and textiles," Adv. Mater. **31**, 1802348 (2018).

[8]D. J. Welker, J. Tostenrude, D. W. Garvey, B. K. Canfield, and M. G. Kuzyk, "Fabrication and characterization of single-mode electro-optic polymer optical fiber," Opt. Lett. **23**, 1826–1828 (1998).

[9]A. F. Abouraddy, M. Bayindir, G. Benoit, S. D. Hart, K. Kuriki, N. Orf, O. Shapira, F. Sorin, B. Temelkuran, and Y. Fink, "Towards multimaterial multifunctional fibres that see, hear, sense and communicate," Nat. Mater. **6**, 336–347 (2007).

[10]F. Sorin, G. Lestoquoy, S. Danto, J. D. Joannopoulos, and Y. Fink, "Resolving optical illumination distributions along an axially symmetric photodetecting fiber," Opt. Express **18**, 24264–24275 (2010).

[11]M. Rein, V. D. Favrod, C. Hou, T. Khudiyev, A. Stolyarov, J. Cox, C.-C. Chung, C. Chhav, M. Ellis, J. Joannopoulos *et al.*, "Diode fibres for fabric-based optical communications," Nature **560**, 214 (2018).

[12]F. Sorin, A. F. Abouraddy, N. Orf, O. Shapira, J. Viens, J. Arnold, J. D. Joannopoulos, and Y. Fink, "Multimaterial photodetecting fibers: A geometric and structural study," Adv. Mater. **19**, 3872–3877 (2007).

[13]S. Egusa, Z. Wang, N. Chocat, Z. M. Ruff, A. M. Stolyarov, D. Shemuly, F. Sorin, P. T. Rakich, J. D. Joannopoulos, and Y. Fink, "Multimaterial piezoelectric fibres," Nat. Mater. **9**, 643–648 (2010).

[14]J. F. Gu, S. Gorgutsa, and M. Skorobogatiy, "Soft capacitor fibers using conductive polymers for electronic textiles," Smart Mater. Struct. **19**, 115006 (2010).

[15]T. Khudiyev, J. Clayton, E. Levy, N. Chocat, A. Gumennik, A. M. Stolyarov, J. Joannopoulos, and Y. Fink, "Electrostrictive microelectromechanical fibres and textiles," Nat. Commun. **8**, 1435 (2017).

[16]Y. Qu, T. Nguyen-Dang, A. G. Page, W. Yan, T. Das Gupta, G. M. Rotaru, R. M. Rossi, V. D. Favrod, N. Bartolomei, and F. Sorin, "Superelastic multimaterial electronic and photonic fibers and devices via thermal drawing," Adv. Mater. **30**, 1707251 (2018).

[17]A. M. Stolyarov, L. Wei, F. Sorin, G. Lestoquoy, J. D. Joannopoulos, and Y. Fink, "Fabrication and characterization of fibers with built-in liquid crystal channels and electrodes for transverse incident-light modulation," Appl. Phys. Lett. **101**, 011108 (2012).

[18]W. Yan, Y. Qu, T. D. Gupta, A. Darga, D. T. Nguyên, A. G. Page, M. Rossi, M. Ceriotti, and F. Sorin, "Semiconducting nanowire-based optoelectronic fibers," Adv. Mater. **29**, 1700681 (2017).

[19]T. Nguyen-Dang, A. C. de Luca, W. Yan, Y. Qu, A. G. Page, M. Volpi, T. D. Gupta, S. P. Lacour, and F. Sorin, "Controlled sub-micrometer hierarchical textures engineered in polymeric fibers and microchannels via thermal drawing," Adv. Funct. Mater. **27**, 1605935 (2017).

[20]Y. Guo, S. Jiang, B. J. B. Grena, I. F. Kimbrough, E. G. Thompson, Y. Fink, H. Sontheimer, T. Yoshinobu, and X. Jia, "Polymer composite with carbon nanofibers aligned during thermal drawing as a microelectrode for chronic neural interfaces," ACS Nano **11**, 6574–6585 (2017).

[21]R. Chen, A. Canales, and P. Anikeeva, "Neural recording and modulation technologies," Nat. Rev. Mater. **2**, 16093 (2017).

[22]E. Pone, C. Dubois, N. Guo, Y. Gao, A. Dupuis, F. Boismenu, S. Lacroix, and M. Skorobogatiy, "Drawing of the hollow all-polymer Bragg fibers," Opt. Express **14**, 5838–5852 (2006).

[23]S. C. Xue, R. I. Tanner, G. W. Barton, R. Lwin, M. C. J. Large, and L. Poladian, "Fabrication of microstructured optical fibers-part I: Problem formulation and numerical modeling of transient draw process," J. Lightwave Technol. **23**, 2245 (2005).

[24]S. Xue, G. Barton, S. Fleming, and A. Argyros, "Heat transfer modeling of the capillary fiber drawing process," J. Heat Transfer **139**, 072001 (2017).

[25]T. Nguyen-Dang, A. G. Page, Y. Qu, M. Volpi, W. Yan, and F. Sorin, "Multimaterial micro-electromechanical fibers with bendable functional domains," J. Phys. D **50**, 144001 (2017).

[26]M. A. Matovich and J. R. Pearson, "Spinning a molten threadline: Steady-state isothermal viscous flows," Ind. Eng. Chem. Fundam. **8**, 512–520 (1969).

[27]Y. T. Shah and J. R. A. Pearson, "On the stability of nonisothermal fiber spinning," Ind. Eng. Chem. Fundam. **11**, 145–149 (1972).

[28]R. German and R. E. Khayat, "Interplay between inertia and elasticity in film casting," J. Fluids Eng. **130**, 081501 (2008).

[29]M. Bechert and B. Scheid, "Combined influence of inertia, gravity, and surface tension on the linear stability of Newtonian fiber spinning," Phys. Rev. Fluids **2**, 113905 (2017).

[30]W. W. Schultz and S. H. Davis, "One-dimensional liquid fibers," J. Rheol. (1978-present) **26**, 331–345 (1982).

[31]B. Scheid, S. Quiligotti, B. Tran, R. Gy, and H. A. Stone, "On the (de)stabilization of draw resonance due to cooling," J. Fluid Mech. **636**, 155–176 (2009).

[32]B. Scheid, E. A. van Nierop, and H. A. Stone, "Thermocapillary-assisted pulling of contact-free liquid films," Phys. Fluids **24**, 032107 (2012).

[33]D. W. Garvey, K. Zimmerman, P. Young, J. Tostenrude, J. S. Townsend, Z. Zhou, M. Lobel, M. Dayton, R. Wittorf, M. G. Kuzyk, J. Sounick, and C. W. Dirk, "Single-mode nonlinear-optical polymer fibers," J. Opt. Soc. Am. B **13**, 2017 (1996).

[34]E. J. Doedel, A. R. Champneys, T. F. Fairgrieve, Y. A. Kuznetsov, B. Sandstede, and X. Wang, "AUTO 97: Continuation and bifurcation software for ordinary differential equations" (1997); AUTO software is freely distributed on http://indy.cs.concordia.ca/auto/.

[35]M. Saphiannikova, T. Skipa, D. Lellinger, I. Alig, and G. Heinrich, "Superposition approach for description of electrical conductivity in sheared MWNT/polycarbonate melts," Express Polym. Lett. **6**, 438–453 (2012).